Novel Single-Point-Type Tactile Pressure Sensors for Earth and Soil-Structure Interface Contact Pressures Measurement

Chang Guo[1] and Chao Zhou[1, 2]

ABSTRACT

The single-point-type tactile pressure sensor (TPS) is a thin and flexible piezoresistive sensor that shows promise in overcoming the limitations of current methodologies for measuring earth pressure within soils and contact pressure at soil-structure interfaces. Despite this potential, the feasibility of the TPS application has not been verified in physical model tests of soil-structure interaction. This paper addresses this gap by introducing a new earth pressure cell (TPS-EPC) with limited thickness and a soil-structure interface contact pressure transducer (TPS-ICPT) conforming to curved interfaces based on a single-point-type TPS. The paper presents a comprehensive methodology encompassing sensor design, signal processing, and calibration. Additionally, a non-linear signal conversion method is recommended to enhance measurement accuracy. Compared to traditional earth pressure cells, TPS-EPCs with the suggested methodology offer more precise earth pressure measurements due to reduced arching effects resulting from their limited thickness. The feasibility of new sensors was validated for the first time in the physical modeling of cyclic axial soil pipe interaction, providing a new and highly sensitive method for soil pressure measurement and yielding valuable insights into soil-pipe interaction behavior, including constrained dilation on the soil-pipe interface and the evolution of soil arching on the pipe.

[1] Department of Civil and Environmental Engineering, The Hong Kong Polytechnic University, Hung Hom, Hong Kong SAR, China, e-mail: chang.guo@connect.polyu.hk; https://orcid.org/0009-0001-7177-9109
[2] Department of Civil and Environmental Engineering; Research Institute for Sustainable Urban Development, The Hong Kong Polytechnic University, Hung Hom, Hong Kong SAR, China (Corresponding author), e-mail: c.zhou@polyu.edu.hk; https://orcid.org/0000-0002-9443-6707

Keywords

Single-point-type tactile pressure sensors; earth pressure cell; soil-structure interface contact pressure transducer; sensor accuracy; soil-structure interaction; physical modeling

Introduction

Tactile pressure sensor (TPS), also known as film-like pressure sensor, is a type of polymer piezoresistive sensor. Its electrical conductance increases with the application of a higher pressure. It could be used to monitor the changes in earth pressure within the soil and contact pressure at the soil-structure interface, which are crucial for understanding the interaction between soil and buried structure. The thickness of traditional earth pressure cells (EPCs) (usually more than 5 mm), coupled with their higher stiffness, may cause soil arching around the sensor, normally leading to an overestimation of earth pressure (Tory and Sparrow 1967, Suits et al. 2005). With a smaller thickness of no more than 0.5 mm, TPS is expected to provide more reliable earth pressure measurement. It is also flexible, allowing it to conform to the curved surfaces of common geotechnical structures like piles and pipes, compared to traditional soil-structure interface contact pressure transducers (ICPT).

TPS can be categorized into two main types based on the number of measuring points: array-type and single-point-type. The array-type TPS typically comprises a grid matrix of small sensing points with the ability to detect hundreds of thousands of measuring points, making it suitable for measuring soil-structure interface contact pressure distribution (Weidlich and Achmus 2008, Palmer et al. 2009, Gillis et al. 2015, Muszynski et al. 2016, Madabhushi and Haigh 2019, Meguid and Ahmed 2020). The single-point-type TPS, on the other hand, has only one sensing area with a diameter or size length ranging from 3 mm to 80 mm (Interlink 2023, Tekscan 2023). The reduced size allows it to avoid altering the surface conditions of structures over a large area. It is also more affordable and can be measured using commonly used dataloggers equipped with an electrical unit that can be easily purchased or even made by users. Therefore, the single-point-

type TPS holds the potential for effectively measuring earth pressure in soil and contact pressure at curved interfaces, thereby enhancing the monitoring of soil-structure interaction.

However, the current utilization of single-point-type TPS mainly focuses on the measurement of contact pressure at flat interfaces in laboratory tests. Kheiripour Langroudi et al. (2010) pasted a single-point TPS on an interface direct shear box to measure the spatial non-uniformities and temporal fluctuations of normal pressure during the interface shear. Gao and Wang (2014) utilized this sensor to measure lateral earth pressure in 1D consolidation testing using an oedometer. The single-point TPS was also developed to measure excess pore water pressure during consolidation using a specialized needle probe. Kootahi and Leung (2022) conducted a study on the size effect of EPC sensing area using the single-point-type TPS in an oedometer. There have been no studies applying the single-point-type TPS in large-scale physical modeling tests or field monitoring. Its feasibility to measure the earth pressure and contact pressure at curved interfaces has not been confirmed. Furthermore, the input-output behavior of TPS exhibits significant non-linearity and hysteresis and is influenced by specific installation conditions (Paikowsky and Hajduk 1997, Muszynski et al. 2016, Liu et al. 2021, Kootahi and Leung 2023). It is necessary to establish a reliable methodology for using the single-point-type TPS that can measure pressures with greater accuracy.

This study introduces a new earth pressure cell (TPS-EPC) and a new soil-structure interface contact pressure transducer (TPS-ICPT), based on the single-point-type TPS, and a corresponding methodology for measuring earth pressure in soils and contact pressures at curved interfaces, respectively. Subsequently, the performance of the TPS-EPC, using the proposed methodology, is compared with that of the traditional EPC in an oedometer. Finally, the feasibility of TPS-based sensors is validated through axial soil-pipe interaction physical modeling.

Design of thin TPS-EPS and curved surface-fitted TPS-ICPT

A typical single-point-type TPS manufactured by Interlink Electronics - Force Sensing Resistor (FSR) 402 was used. The active area has a diameter of 12.7 mm, which is larger than 30 d_{50} of the sand used in this study, sufficiently avoiding the particle size effects on the measurement accuracy based on the results of Kootahi and Leung (2022). The nominal thickness of the sensor is 0.46 mm, no more than 1.25 d_{50} of the sand used in this study. More details can be found in Interlink (2023).

Two new transducers (i.e., TPS-EPC and TPS-ICPT) were developed. Fig. 1 (a) and Fig. 1 (b) show a schematic diagram and photograph of the TPS-EPC. TPS could not be buried in the soil directly because the soil deformation may stretch or bend the flexible sensors, resulting in an unpredictable effect on the TPS's sensitivity and zero offset (Interlink 2023). Therefore, TPS is stuck on a 0.5-mm-thickness insulating-paint coated steel slice whose shape adapts to TPS via water-cutting. Meanwhile, a coating layer by Epoxy Adhesive DP100 manufactured by 3M^{TM} is utilized to protect the TPS. After 48 hours of curing, the epoxy adhesive would form a stiff coating layer with a thickness of around 0.5 mm. The coating would affect the sensitivity of TPS. Eighteen coated TPS-based sensors were calibrated with a loading path of 0~60 kPa and a pressure loading rate of 4 kPa/min. Their average sensitivity is 7.75 $(\text{GPa}\cdot\Omega)^{-1}$, which is sufficiently sensitive for measuring earth and soil-structure interface pressures. More details of calibration are discussed later. The short tail version of FSR 402 (FSR 402 Short) is used in TPS-EPC for a smaller volume. A heat shrink tube is set at the tail of TPS and steel slice to further protect the wiring position. The outsides of the slice's tail have a couple of grooves for better fixing the heat shrink tube. The thickness of the new sensor is around 1.5 mm, equaling 4 d_{50} of the sand used in this study,

significantly smaller than the thickness of the commonly used earth pressure cell. The effect of soil arching on TPS-EPC is verified and compared with traditional EPC later.

The schematic diagram and photograph of the TPS-ICPT on a pipe surface are illustrated in Fig. 1 (c) and Fig. 1 (d). The long-tail version of FSR 402 is used in TPS-ICPT for better wiring. Holes with a diameter of 8 mm are opened on the pipe. After wiring through the holes, the FSR 402 is stuck on the pipe surface by making use of its flexibility and coated using the same method in TPS-EPC. The total thickness of FSR 402 and the epoxy coating is around 0.5 mm, close to d_{50} of the sand used in this study. Hence, the effect of thickness is negligible.

Based on the results of some trial tests, the threshold pressure that induces an obvious change in the electrical conductance (>1 MPa^{-1}) of bare FSR 402 varies from 0~10 kPa. Increasing the surface roughness of the pipe or steel slice was found to be able to reduce the threshold pressure to almost zero in all cases. The working principle of this method is probably due to the more significant prestressing during the sticking process for a rougher surface. The surface roughness can be controlled using mechanical surface treatment technology directly or mixing some silty soil evenly into the epoxy adhesive used between TPS and the surface of the pipe or slice.

Multi-channel measurement

The output signal of single-point-type TPS is its electrical conductance (G) (the reciprocal of electrical resistance (R)). It cannot be directly measured by common data loggers used in geotechnical testing.

Fig. 2 (a) shows a method suggested by Interlink (2023) and used in some other studies (Gao et al. 2017). This method adds an amplifier (denoted as *Amp.* in the figure) and a trimmer resistor with a constant and known resistance $R_{\text{Trimmer.}}$ The resultant electrical interface could

convert the electrical conductance signal to a voltage signal. The electrical conductance of TPS can be calculated as follows:

$$G_{\mathrm{TPS}} = -\frac{V_{\mathrm{out}}}{R_{\mathrm{Trimmer}} V_{\mathrm{ref}}} \tag{1}$$

where V_{out} is the output electrical voltage and V_{ref} is the input reference electrical voltage. The processes of wiring and debugging using this method are troublesome and complicated. Hence, this method is suitable for cases where the number of measurement targets is limited.

Fig. 2 (b) is a newly proposed method that is more convenient and available for a large number of measurement targets. This method is based on a specific data logger - dataTaker DT85 manufactured by Thermo Fisher. Compared to other common data loggers in geotechnical testing, dataTaker DT85 can measure the electrical resistance (the reciprocal of electrical conductance) directly using the 4-wire Kelvin method via the corresponding module that has been embedded in the dataTaker DT85. Users can easily connect the TPSs to dataTaker DT85, as illustrated in Fig. 2 (b). One problem found by the authors is that the measurement is easily affected by electromagnetic interference from electromechanical apparatuses in the experimental environment. It is because the default 4-wire Kelvin method excitation current in dataTaker DT85 for the electrical resistance range of TPS (normally 0.1~100 kΩ) is as weak as 2 or 200 μA. To minimize the effect of electromagnetic interference, a stronger excitation current of 2.5 mA (I_0 in Fig. 2 (b), optional in dataTaker DT85) is suggested to be used. However, it would limit the maximum resistance measurement range to 700 Ω. Thus, a resistor with a resistance, R_0, of 700 Ω is suggested to be in parallel with TPS. Then, the electrical conductance of the TPS could be calculated as

$$G_{\mathrm{TPS}} = \frac{1}{R_{\mathrm{TPS}}} = \frac{1}{R_{\mathrm{out}}} - \frac{1}{R_0} \tag{2}$$

where R_{out} is the output electrical resistance value. Meanwhile, common methods, such as using a grounding system and shielded twisted pair cables, should also be employed to eliminate electromagnetic interference.

DT85 also has an advantage in multi-channel measurement. One set of DT85 Series 4 is available for the measurement of sixteen electrical resistance signals, simultaneously. Coupled with the channel expansion module, CEM20, the maximum number of electrical resistance signal measurements is expandable to 320. In the physical modeling of this study, there are twenty-two TPS-based sensors, including four TPS-EPCs and eighteen TPS-ICPTs, and thus, one set of DT85 Series 4 and one set of CEM20 are used.

Post-installation calibration of TPS-EPC and TPS-ICPT

The performance of TPS highly depends on specific installation conditions. Hence, calibration after installation is necessary. A sealed tank is used for the calibration of TPS-EPCs. TPS-EPCs are put inside of the tank and its wire exits through sealed joints. During calibration, the air pressure can be controlled using a pneumatic regulator with a preset pressure path.

As for TPS-ICPTs, modified pipe repair clamps are utilized, as shown in Fig. 3. The pipe repair clamp, consisting of a rubber sleeve with thickened edges and a steel split sleeve with screws, was originally used for repairing leaking pipes. A through hole is punched in the middle of the repair clamp and is connected hermetically with a pneumatic connector. Hence, a sealed space that can control the air pressure is formed on the pipe surface with TPS-ICPTs (see Fig. 3(b)). Teflon tape and heat shrink tubing can be used to prevent gas leakage between the pipe and the edges of the repair clamp's rubber sleeve. Using a similar method of controlling pressure as for TPS-EPC, the relationship between applied pressure and output can be determined.

Fig. 4 shows the typical results of the electrical conductance evolution over elapsed time for TPS-EPC and TPS-ICPT. The air pressure was increased stepwise from 0 to 200 kPa (loading path), a typical range in geotechnical engineering, and then reverted to 0 kPa (unloading path), in a total of 17 stages. At each stage, the pressure was swiftly adjusted and sustained for a duration of $\Delta P/v$, where ΔP represents the variation in air pressure and v signifies the loading rate, equaling 4 kPa/min. Fig. 5 (a) and Fig. 6 (a) illustrate the results from Fig. 4, showing the relationship between electrical conductance and pressure during the loop path and the loading and unloading paths, respectively. The data points for the loading and unloading paths in Fig. 6 (a) represent the outputs at the end of each stage in Fig. 4, while the data for the loop path in Fig. 5 (a) are the mean values of calibration results under the same pressure during loading and unloading paths.

Three key characteristics can be observed in Fig. 4, Fig. 5 (a), and Fig. 6 (a). Firstly, the electrical conductance of the TPS rises and falls with pressure. However, the curves representing the relationship between electrical conductance and pressure are non-linear, with their slopes diminishing as pressure increases. Secondly, a noticeable hysteresis is present in the loop of the electrical conductance-pressure curves. Although the outputs revert to nearly initial values when the pressure is regulated to zero, the electrical conductance during the unloading path is typically higher than that during the loading path. The behavior observed during the unloading path is linked to the maximum calibration pressure. Thirdly, a short-term drift is evident in each stage, especially during the loading path. Despite the TPS's rapid response to pressure changes (less than 3 microseconds as stated in Interlink (2023)), the output value of electrical conductance continues to rise over time. Post-installation calibration of eighteen TPS-based sensors (comprising fifteen TPS-ICPTs and three TPS-EPCs) regarding these features are provided below.

The non-linearity of a sensor can be gauged by its non-linearity error. As depicted in Fig. 5 (a), calibration data can be fitted using the best-fit straight line (BSL): $G=kP+G_0$, where P represents the output value of pressure, G is the measured electrical conductance, k is sensitivity, and P_0 is the zero offset of the sensor. The non-linearity error is defined as the percentage of the maximum output deviation between the calibration curve and its BSL to the maximum output range, as outlined by Nyce (2004). Fig. 5 (b) presents the average non-linearity error of the loading path based on the calibration results of eighteen TPS-based sensors with a pressure loading rate of 4 kPa/min. The non-linearity errors of the unloading and loop path (calculated using values of the mean of calibration results under the same pressure during loading and unloading paths) are also depicted. The non-linearity error escalates with the maximum calibration pressure, irrespective of the path. The values of the three paths increase from 4.2 to 5.8 %, 11.2~17.2 %, and 7.3~11.2 %, respectively. The calibration results under the loading path exhibit the best linearity. The standard errors of the average non-linearity errors are no more than ± 8.4‰.

Fig. 6 depicts the hysteresis errors with varying calibration pressures based on the calibration results of eighteen TPS-based sensors. The hysteresis error is defined as the ratio of the maximum output deviation between the loading and unloading paths to the output range, as shown in Fig. 6 (a). Although the effect of maximum pressure is not significant, the values are as high as at least 10 % (see Fig. 6 (b)).

Both the non-linearity error and hysteresis error contribute to the sum static error, which is a crucial measure of a sensor's performance. The sum static error, e_{sum}, of a sensor is normally estimated using the root-sum-of-squares (RSS) method with $e_{\text{sum}} = \sqrt{\sum_{j=1}^{n} e_j^2}$, where e_j is an individual error (i.e., non-linearity error or hysteresis error in this case) and n is the number of errors. Therefore, based on the above results, the TPS's sum static error could reach up to 22%. It

might be difficult to minimize this sum static error based on the current TPS technique. However, utilizing the non-linear signal conversion method recommended in the following section could be helpful to improve measurement accuracy.

Fig. 7 illustrates the typical calibration results of a TPS-ICPT with different loading rates. Three loading rates, 1, 4, and 10 kPa/min, which are estimated as the values in the following physical modeling, were selected. The maximum calibration pressure is 60 kPa. The electrical conductance of each stage increases with the loading rate, which is consistent with the results in Fig. 4. The calibration results of eighteen TPS-based sensors indicate that as the loading rate increases from 1 to 10 kPa/min, the average sensitivity experiences a decrease from 8.61 to 7.25 $(GPa \cdot \Omega)^{-1}$, while the average zero offset decrease around 7 $M\Omega^{-1}$.

Non-linear signal conversion

The relationship between the physical quantity being measured and the output signal of common geotechnical sensors, such as pore pressure transducers and linear variable displacement transducers, is normally highly linear within its measurement range. Thus, the results of the output signal are normally converted into physical quantity based on the fitted BSL. However, the performance of the TPS-based sensor is not ideal, according to the calibration results above. To improve its accuracy, a non-linear signal conversion method is suggested to be used. After calibrating the sensor, its electrical conductance-pressure relationship is fitted using the smoothing spline algorithm in MATLAB's Curve Fitting app. Then, the results of electrical conductance measured during experiments can be input into this relationship to return the results of pressure on the sensor. Utilizing the non-linear signal conversion method and selecting a conductance-pressure curve calibrated under a condition close to the measurement could eliminate the effect of non-

linearity error and minimize the effect of the hysteresis error. Consequently, the deviation caused by the sum static error might be less than 7.1 %.

The loading range and rate in the calibration should be as close as possible to the experimental condition. If the measured pressure is increasing, the calibration results under the loading path should be used as the reference for signal conversion. For the unloading path, aside from the non-linearity, the curve of the unloading path is highly dependent on the maximum calibration pressure and is only reliable when the maximum calibration pressure is close to the maximum pressure in the experiment. Conversely, if the measured pressure continually fluctuates, the calibration results of the loop path may serve as a better reference.

Comparison between traditional EPC and TPS-based EPC

As previously mentioned, the large thickness of traditional EPC can lead to stress concentration due to arching when they are buried inside the soil. Hence, the earth pressure measured by them is higher than the actual value. The TPS-based EPC, with a limited thickness, can significantly minimize this problem. To quantify this effect, three calibration tests were conducted using a modified oedometer, as illustrated on the right side of Fig. 8. A piezoelectric-ceramics-based EPC with a thickness (height) of 10 mm and a diameter of 20 mm represents the traditional EPC. Its nominal maximum pressure is 100 kPa with a static error of no more than 0.4%. In Condition I, the traditional EPC was embedded in the baseplate of the oedometer to create an ideal condition with no EPC thickness and compared to Conditions II and III, where the traditional EPC and TPS-EPC were placed on the baseplate of the oedometer to simulate the buried conditions in the experiment and practice.

The testing soil used in this study is standard medium sand sourced from Fujian Province, China, with a particle size ranging from 0.25 to 0.5 mm. The parameters of this sand are provided in TABLE 1. The dimensions of the soil specimen inside the oedometer are 40 mm in height and 70 mm in diameter. The specimens were compacted in layers of 10 mm with a relative density of 85%. After that, the specimen was loaded in stages. Each stage lasted at least two minutes until the readings of settlement and pressure were stable.

Fig. 8 illustrates the experimental results. In Condition I, the measured pressures are consistent with pressures applied on the top of the specimen, confirming the good performance of the traditional EPC when there is no thickness effect and piezoelectric ceramics utilized by the selected traditional EPC is a mature technique in pressure measurement. The measured pressures in Condition II exhibit a linear relationship with applied pressures, but the former is approximately 80% larger than the latter. This difference demonstrates the significant influence of the traditional EPC's thickness. As for Condition III, the measured pressure is slightly higher than the applied values at early loading stages and then approaches the applied value at later stages. Its error is no more than 10%, demonstrating the good performance of TPS-based sensors compared to traditional EPCs.

To understand the results of oedometer tests, 3D discrete element modeling (DEM) was carried out to interpret the experimental results. The simulation was conducted using the open-source code YADE (Kozicki and Donzé 2008). A six-wall box was established as the boundary to model the oedometer cell. Another six-wall box set in the middle of the boundary bottom wall represented the sensor. The dimensions of the boundary and sensor model were the same as those of the experiments. The shapes of the boundary and the sensors were cuboid rather than cylinders for easier modeling. The linear elastic-friction model (Šmilauer and Chareyre 2021) is used to

simulate the particle-particle and particle-wall contacts, which requires three input parameters including Young's modulus, the ratio of shear to normal stiffness, and the contact friction angle. The model parameters used in this study are calibrated against the direct shear tests on the sand used in this experiment and summarized in TABLE 2. Approximately 30,000 particles with uniform diameters were randomly generated and were compacted to the target relative density (85%) using the radius expansion method (Scholtès et al. 2009). The final particle diameter was around 1.88 mm, consistent with 5 times the mean particle size in the experiment. Finally, the normal pressure on the specimens was controlled using the top wall of the boundary cuboid. The specimens were also loaded by stages. Each stage continued until the top pressure reached the target, and the unbalanced force was less than 0.1%.

The computed pressures are also shown in Fig. 8 for comparison. The trends observed in experiments are all confirmed by the numerical results, although the computed and measured results are slightly different. The arching effect mechanism can be analyzed using the DEM simulation results. Fig. 9 illustrates the vertical displacement of soil particles as the applied top pressure increases from 0 to 100 kPa. All the values are negative due to soil compaction as pressure increases. Fig. 10 shows the projection of the strong force chain network in the DEM simulation of Conditions I to III. The strong force chain is a chain network of contact normal forces larger than their median values (Peters et al. 2005). The thickness of each chain is proportional to the magnitude of force. For clear distinction, only the data from particles between the sensor's front and rear walls are shown in Fig. 9 and Fig. 10. In Condition I shown in Fig. 9 (a), the vertical settlements (negative values of vertical displacement) of particles decrease from around 150 μm to 0 μm with increasing depth, and all settlements are uniform at the same depth. Correspondingly, the force chains in Condition I (see Fig. 10 (a)) distribute uniformly in the space, with the

maximum contact normal force of 2.12 N, proving that the soil particles support the loading from the top wall evenly. As for Condition II, the particle settlements above the sensor's top wall are smaller than those on the left and right sides due to varying soil thickness (see Fig. 9 (b)). This non-uniform settlement indicates a relative displacement, applying an additional downward force above the sensor's top wall with stronger force chains (maximum contact normal force = 3.08 N, see Fig. 10 (b)). This corresponds to the higher measured pressures shown in Fig. 8. By comparison, non-uniform particle displacement and the concentration of the force chain (2.16 N in maximum) on the sensor top wall in Condition III (see Fig. 9 (c) and Fig. 10 (c)) is not as obvious as that of Condition II, causing a limited difference between the measured and applied pressures in Fig. 8.

Based on the above tests and DEM simulations, the limited thickness of the TPS-EPC can reduce the error caused by the arching effect on the sensors from around 80% to no more than 10% when the sensor is buried inside of the soil, demonstrating a more accurate measurement of earth pressure. Furthermore, in the practice of field or physical modeling, the soil around the buried sensors can be disturbed during sensor installation. Compared to the traditional commercial EPC, the TPS-EPC, with its smaller volume and mass, would cause fewer disturbances.

Application in Physical Modelling of Axial Soil-pipe Interaction

EXPERIMENTAL SYSTEM, MATERIAL, AND METHOD

The feasibility of TPS-based sensors application in physical modeling was verified in a cyclic axial soil-pipe interaction test utilizing the apparatus in Fig. 11. This apparatus comprised a steel box, a steel pipe, an axial actuation subsystem, and a vertical loading subsystem. Two holes are located on the front and rear walls at a height of 0.35 m, allowing the pipe to pass through and maintain a consistent soil-pipe interaction length during the test. A seamless steel pipe, typically

used in Hong Kong's natural gas and water pipeline system, with a nominal outer diameter of 102 mm and a nominal thickness of 4 mm, was employed (BSI 2002, WSD 2020). The pipe surface underwent a turning method treatment with a depth of 0.38 mm and an interval of 0.9 mm to obtain a normalized roughness ($R_n = R_{max} / d_{50}$, Kishida and Uesugi (1987)) of 1.01. Further details are summarized in TABLE 3.

The axial actuation subsystem, which comprises a servo-electric linear actuator and a reaction frame, was designed to regulate axial displacement. The pipe was engineered to move freely in the vertical direction during its axial movement, facilitated by a connector depicted in the front view of Fig. 11. A flexible pneumatic bag was positioned between the soil's upper surface and the top cap. The length and width of the pneumatic bag are designed to fit the interior dimensions of the box. The bag's top surface has two holes: one for connection to a pneumatic regulator and the other for an air pressure gauge. A top cap, reinforced with beams, was installed above the pneumatic bag and the box to provide a reaction force. The nominal pressure at the crown, σ_c', can be manipulated by adjusting the air pressure P inside the bag, using the formula $\sigma_c' = \gamma' H_{c0} + P$, where H_{c0} (= 0.36 m) represents the actual buried depth from the ground surface to the pipe's crown. The target nominal pressure σ_c' in this study is 34 kPa, equivalent to 2 m in burial depths.

Eighteen TPS-ICPTs were placed across three cross-sections of the pipe, with a spacing of 0.4 m between each section. On each cross-section, six TPS-ICPTs were installed at the crown, one shoulder, two springlines, one haunch, and the invert, as indicated by red points in Fig. 11. Four TPS-EPCs were employed to measure overburden pressures at various positions (see the side view of Fig. 11). Four traditional EPCs, based on piezoelectric ceramics, were buried in the same distribution as the TPS-EPCs for comparison. All TPS-based sensors were calibrated under a loop

path of 0-200 kPa. The loading path curves were used as a reference during the first loading (the loading process of the first cycle), as the pressures were primarily increasing. After the first loading, the loop path curves were used for conductance-pressure conversion due to repeated increases and decreases. Additionally, a load cell with a measurement range of ± 10,000 N and an LVDT with a measurement range of 50 mm were installed between the pipe and the loading system to monitor the axial force and axial displacement, respectively.

The sand used in this study is medium sand from Fujian Province, with a particle size of 0.25 to 0.5 mm. More details of this sand are summarized in TABLE 1. The target relative density for the study is set at 85%, as per the compaction requirement for backfilling pipeline trenches in practice (USBR 1996, WSD 2012). The sand pluviation method was used to prepare dense and uniform samples (Rad and Tumay 1985, Fretti et al. 1995, Tabaroei et al. 2017).

After preparing the soil sample and placing the pneumatic bag on the soil, it was covered with the top cap. The air pressure was then set to the desired value and maintained for around 30 minutes until sensor readings, such as vertical displacement and earth pressure, became stable. The pipe was subjected to axial loading at a speed of 0.02 mm/s. Five one-way cycles with an amplitude of 20 mm were applied. More details of the experimental system and methodology can be seen in (Guo and Zhou 2024).

RESULTS AND DISCUSSION

Performance of TPS-ICPT

Fig. 12 depicts the evolution of interface contact pressures as measured by TPS-ICPTs. The discrepancy in interface contact pressures at corresponding positions across the three cross-sections is generally within 10% of the average value. Consequently, the average values of the three cross-sections are directly displayed in Fig. 12. The difference in interface contact pressure

between the left and right springlines (see Fig. 12) remains below 4 kPa during cycling, indicating good symmetry. Therefore, the average value of the left and right springlines is used as the results of the springline in the subsequent analysis.

Before the test, the pressure at the invert exceeds 34 kPa, the nominal pressure at the crown σ_c'. This could be attributed to the soil arching effect on the pipe, which is similar to the results of the arching effect on traditional EPC, as shown in Fig. 8 and Fig. 9. The stiffer pipe results in uneven deformation around the pipe, causing soil above and below the pipe to experience relative displacement to the soil on the sides of the pipe. This results in higher interface contact pressure in the vertical direction of the pipe.

During each pullout process, there is a noticeable increase in the interface contact pressures. This is attributed to the constrained dilation behavior observed at the soil-pipe interface. Specifically, the tendency of soil dilation increases the interface contact pressures (Ng et al. 2020). The increase in pressures is particularly significant at the crown and invert, reaching 56.8 and 68.9 kPa during the first loading. The dilation between the soil-pipe interface may also cause additional relative displacement in the vertical direction, leading to further soil arching and thus an additional increase in pressure at the pipe's crown and invert. The interface contact pressures reduce to 3~12 kPa in each initial phase of the loading direction reverse, which is due to the re-establishment of the force chain.

After the first loading, the magnitude of interface contact pressures and their fluctuation range noticeably decrease. This could be due to the degradation of interface dilation during cycling and the disappearance of the arching-related strong force chain during the initial phase of the loading direction reverse. The evolution of pressures at different positions on the pipe during cycling does not follow a regular fluctuation pattern, which could be due to the inevitable

misalignment of the pipe and the axial actuation subsystem. However, the average interface contact pressure, as shown by the thick black curve in Fig. 12, displays a very regular pattern of fluctuations between 7 to 23 kPa after the first loading. The aforementioned evolution process of interface contact pressures measured by TPS-ICPT is reasonable, thereby validating the efficiency of TPS-ICPT.

The stress path at the soil-pipe interfaces, as illustrated in Fig. 13, further substantiates the rationality of TPS-ICPTs' results. The vertical axis of Fig. 13 represents the average axial resistance per unit area, calculated by the axial force measured by the load cell. Failure envelopes of steel interfaces with the same surface treatment method are determined through constant normal loading (CNL) interface direct shear testing and are included as references in Fig. 13. The stress path shape of the first loading is similar to the typical stress path of constant normal stiffness (CNS) interface shear tests by Pra-ai and Boulon (2016). It rises vertically and then turns to the top left due to the constrained dilation, as mentioned above. After touching the peak interface friction envelope, the path turns to and stops at the critical state envelope. The interface contact pressures decrease at the initial phase of the first unloading, causing the path to swiftly move to the left of the horizontal axis. Subsequently, the path gradually approaches the critical state envelope and develops to larger resistance and interface contact pressure along it. The stress paths of the following cycles have similar shapes to the first unloading and slightly move left with cycles. The evolution of the stress path illustrates that the maximum interface shear angle transforms from the peak interface shear angle to the critical state interface shear angle and finally stabilizes in the latter.

Performance of TPS-EPC

Fig. 14 compares the evolution of vertical earth pressures as measured by TPS-EPCs and traditional EPCs. The overburden pressure without considering stress redistribution, σ_e', can be calculated by $\sigma_e' = \gamma' H_0 + P$, where H_0 is the buried depth from the ground surface to the sensor.

Fig. 14 (a) illustrates the earth pressures at a point 0.5 D higher than the pipe crown (position #1 in the side view of Fig. 11). Before the test, the pressure measured by TPS-EPC #1 was 35 kPa, which is slightly larger than σ_e' and the interface contact pressure at the pipe crown. As the pipe moved, the pressure increased by approximately 15 kPa due to the further arching effect and the pressure increase induced by the constrained dilation on the pipe. In subsequent cycles, the earth pressure increased during each loading and decreased during each reverse of the loading direction. With cycles, the measured values gradually decreased and approached σ_e', and the fluctuation amplitude decreased. This trend demonstrated the degradation of soil arching and constrained dilation. The behavior of TPS-EPC #1 is consistent with the results of TPS-ICPT and its values keep in a reasonable range. In contrast, the values measured by traditional EPC #1 reported unreliable values. Before the test, the pressure measured was 76 kPa, which is significantly larger than the estimated value. Subsequently, the pressure measured by the traditional EPC increased significantly to more than 120 kPa as the pipe continued to move. In the following cycles, the fluctuation of earth pressure measured by traditional EPC #1 remained high. From the third cycle, the earth pressure during the loading direction reverse reached 0 kPa. It might be because the continuous disturbance on the traditional EPC caused the soil around the sensor to loosen, causing no touch during the loading conversion.

Fig. 14 (b) demonstrates the vertical pressure evolution at 0.5 D lower than the pipe invert (position #2 in the side view of Fig. 11). TPS-EPC #2 displayed similar behavior to TPS-EPC #1, with its values fluctuating around σ_e' from the first unloading, albeit with a slightly larger

amplitude. On the other hand, the pressure recorded by the traditional EPC seems unreasonable as it starts at 59 kPa, which is significantly higher than σ_e'. Subsequently, the earth pressure drops to 2.3 kPa during the next loading direction reverse, indicating excessive volatility.

Fig. 14 (c) and (d) show the vertical pressure evolution at the position of 1.5 D to the left of the pipe center. The horizontal positions of EPCs in Fig. 14 (c) and (d) (#3 and #4 in the side view of Fig. 11) are at the pipe center and 1.5 D higher than the pipe center, respectively. The testing results for TPS-EPC #3 and #4 exhibit contrasting behaviors to those of TPS-EPC #1 and #2. Firstly, before the test, values of TPS-EPC #3 and #4 were smaller than their σ_e'. Secondly, during the cycle, the pressures experienced decrease during each loading and unloading while increasing upon each reverse in the loading direction. Thirdly, the fluctuation amplitude gradually decreased but the outputs tended to approach σ_e'. These observations of TPS-EPC #3 and #4 further confirm the soil arching evolution, wherein the arching effect concentrates the overburden pressure on the pipe and simultaneously reduces the vertical pressure in the soil on the left and right sides of the pipe. In contrast, the outputs of traditional EPC decreased during cycles instead of approaching σ_e'. It is also potentially due to soil loosening caused by external disturbances.

Conclusions

This paper introduces a new earth pressure cell (TPS-EPC) and a new soil-structure interface contact pressure transducer (TPS-ICPT), both based on a single-point-type tactile pressure sensor. The performance of TPS-based sensors is assessed and applied to a cyclic axial soil-pipe interaction physical model. The primary conclusions are as follows:

The performance of TPS is contingent on its specific installation conditions. Therefore, post-installation calibration is crucial for TPS-based sensors. Furthermore, the sum error of TPS

on non-linearity and hysteresis could reach up to 22% based on the BSL of calibration results. The loading rate of pressure also influences the sensitivity and zero offset of TPS-based sensors. Utilizing the non-linear signal conversion method and selecting a conductance-pressure curve calibrated under conditions close to the experiment can optimize accuracy.

TPS-ICPTs performed commendably in the cyclic axial soil-pipe interaction physical model. The evolution of interface contact pressures' distribution demonstrated a coupling process of soil arching effect on the pipe and the constrained dilatancy behavior on the soil-pipe interface. The average interface contact pressure exhibits a consistent pattern of fluctuations after the first loading. The stress path transitions from the peak interface shear envelope to the critical state interface shear envelope. The above proves the reliability of the results of interface contact pressures measured by TPS-ICPTs.

A comparison between TPS-EPC and traditional EPC in a modified oedometer and a corresponding 3D DEM simulation. The results reveal that traditional EPC, when buried inside the soil, is significantly affected by its thickness, leading to an 80% overestimation of the applied pressure due to the soil arching effect on the sensor. In contrast, the limited thickness of TPS-EPC can minimize the arching effect on the sensors, resulting in a more accurate earth pressure measurement with an error of no more than 10%. In the physical modeling, the vertical earth pressures measured by traditional EPCs fluctuated excessively. This might be due to the more pronounced arching effect on the sensor and the disturbance of soil around the sensor during pipe movement. Conversely, the values measured by TPS-EPC fluctuated around the estimated pressure and were reasonably affected by the evolution of soil arching on the pipe.

ACKNOWLEDGEMENTS

The authors would like to thank the Research Grants Council (RGC) of the HKSAR for providing financial support through grant N_PolyU526/23 and AoE/E-603/18. This work is also supported by RISUD/PolyU under Grant 1-BBWS.

References

BSI. 2002. *Seamless and welded steel tubes. Dimensions and masses per unit length.* BSI EN 10220:2002. London, UK: BSI Group, approved December 13, 2002. https://web.archive.org/web/20240319182924/https://webstore.ansi.org/standards/bsi/bsen102202002

Fretti, C., D. C. F. Lo Presti, and S. Pedroni. 1995, "A Pluvial Deposition Method to Reconstitute Well-Graded Sand Specimens." *Geotechnical Testing Journal* 18, no. 2 (June): 292-298. https://doi.org/10.1520/GTJ10330J

Gao, Y. and Y. H. Wang. 2014, "Experimental and DEM Examinations of K0 in Sand under Different Loading Conditions." *Journal of Geotechnical and Geoenvironmental Engineering* 140, no. 5 (February): 04014012. http://doi.org/10.1061/(asce)gt.1943-5606.0001095

Gao, Y., Y. H. Wang, and J. K. Chow. 2017, "Application of Film-Like Sensors for K0 and Pore Water Pressure Measurement in Clay During 1D Consolidation." *Geotechnical Testing Journal* 40, no. 1 (January): 134-143. http://doi.org/10.1520/GTJ20160008

Gillis, K., S. Dashti, and Y. M. A. Hashash. 2015, "Dynamic Calibration of Tactile Sensors for Measurement of Soil Pressures in Centrifuge." *Geotechnical Testing Journal* 38, no. 3 (May): 261-274. https://doi.org/10.1520/GTJ20140184

Guo, C. and C. Zhou. 2024, "Axial behaviour of steel pipelines buried in sand: effects of surface roughness and hardness." *Géotechnique* (October, published online): 1-14. https://doi.org/10.1680/jgeot.24.00001

Interlink. 2023. "FSR® Integration Guide & Evaluation Parts Catalog With Suggested Electrical Interfaces." Interlink Electronics. http://www.tinyos.net.cn/datasheet/fsrguide.pdf

Kheiripour Langroudi, M., J. Sun, S. Sundaresan, and G. I. Tardos. 2010, "Transmission of stresses in static and sheared granular beds: The influence of particle size, shearing rate, layer thickness and sensor size." *Powder Technology* 203, no. 1 (October): 23-32. https://doi.org/10.1016/j.powtec.2010.03.028

Kishida, H. and M. Uesugi. 1987, "Tests of the interface between sand and steel in the simple shear apparatus." *Géotechnique* 37, no. 1 (March): 45-52. https://doi.org/10.1680/geot.1987.37.1.45

Kootahi, K. and A. K. Leung. 2022, "Effect of Soil Particle Size on the Accuracy of Tactile Pressure Sensors." *J. Geotech. Geoenviron. Eng* 148, no. 10 (August): 06022008. https://doi.org/10.1061/(asce)gt.1943-5606.0002899

Kootahi, K. and A. K. Leung. 2023, "Evaluating the Performance of Flexible Piezoresistive Sensors for Measuring Static Contact Stress." *Geotechnical Testing Journal* 46, no. 1 (January): 68-103. https://doi.org/10.1520/GTJ20210197

Kozicki, J. and F. V. Donzé. 2008, "A new open-source software developed for numerical simulations using discrete modeling methods." *Computer Methods in Applied Mechanics and Engineering* 197, no. 49 (September): 4429-4443. https://doi.org/10.1016/j.cma.2008.05.023

Liu, K. Y., C. S. Xu, and X. L. Zhang. 2021, "Measurement Performance Evaluation of Tactile Pressure Sensor with Different Particle Sizes and Sensor Curvatures." *Geotech. Test. J* 44, no. 4 (July): 1036-1054. https://doi.org/10.1520/GTJ20200028

Madabhushi, S. S. C. and S. K. Haigh. 2019, "Using tactile pressure sensors to measure dynamic earth pressures around dual-row walls." *International Journal of Physical Modelling in Geotechnics* 19, no. 2 (March): 58-71. https://doi.org/10.1680/jphmg.17.00053

Meguid, M. A. and M. R. Ahmed. 2020, "Earth Pressure Distribution on Buried Pipes Installed with Geofoam Inclusion and Subjected to Cyclic Loading." *International Journal of Geosynthetics and Ground Engineering* 6, no. 2 (March): 1-8. https://doi.org/10.1007/s40891-020-0187-5

Muszynski, M. R., S. M. Olson, Y. M. A. Hashash, and C. Phillips. 2016, "Earth Pressure Measurements Using Tactile Pressure Sensors in a Saturated Sand During Static and Dynamic Centrifuge Testing." *Geotechnical Testing Journal* 39, no. 3 (May): 371-390. https://doi.org/10.1520/GTJ20150049

Ng, C. W. W., C. Zhou, and C. F. Chiu. 2020, "Constitutive modelling of state-dependent behaviour of unsaturated soils: an overview." *Acta Geotechnica* 15, no. 10 (July): 2705-2725. https://doi.org/10.1007/s11440-020-01014-7

Nyce, D. S. 2004. *Linear position sensors: theory and application*, Hoboken, NJ: John Wiley & Sons. http://doi.org/10.1002/0471474282

Paikowsky, S. G. and E. L. Hajduk. 1997, "Calibration and Use of Grid-Based Tactile Pressure Sensors in Granular Material." *Geotechnical Testing Journal* 20, no. 2 (June): 218-241. https://doi.org/10.1520/GTJ10741J

Palmer, M. C., T. D. O'Rourke, N. A. Olson, T. Abdoun, D. Ha, and M. J. O'Rourke. 2009, "Tactile Pressure Sensors for Soil-Structure Interaction Assessment." *Journal of Geotechnical and Geoenvironmental Engineering* 135, no. 11 (October): 1638-1645. https://doi.org/10.1061/(asce)gt.1943-5606.0000143

Peters, J., M. Muthuswamy, J. Wibowo, and A. Tordesillas. 2005, "Characterization of force chains in granular material." *Physical Review E* 72, no. 4 (October): 041307. https://doi.org/10.1103/PhysRevE.72.041307

Pra-ai, S. and M. Boulon. 2016, "Soil–structure cyclic direct shear tests: a new interpretation of the direct shear experiment and its application to a series of cyclic tests." *Acta Geotech* 12, no. 1 (July): 107-127. https://doi.org/10.1007/s11440-016-0456-6

Rad, N. S. and M. T. Tumay. 1985, "Factors Affecting Sand Specimen Preparation by Raining." *Geotechnical Testing Journal* 10, no. 1 (March): 31-37. https://doi.org/10.1520/GTJ10136J

Scholtès, L., P. Y. Hicher, F. Nicot, B. Chareyre, and F. Darve. 2009, "On the capillary stress tensor in wet granular materials." *International Journal for Numerical and Analytical Methods in Geomechanics* 33, no. 10 (January): 1289-1313. https://doi.org/10.1002/nag.767

Šmilauer, V. and B. Chareyre. 2021. *Yade Documentation*, 3rd ed. Online: The Yade Project. http://doi.org/10.5281/zenodo.5705394

Suits, L., T. Sheahan, J. Labuz, and B. Theroux. 2005, "Laboratory Calibration of Earth Pressure Cells." *Geotechnical Testing Journal* 28, no. 2 (March): 188-196. https://doi.org/10.1520/GTJ12089

Tabaroei, A., S. Abrishami, and E. S. Hosseininia. 2017, "Comparison between Two Different Pluviation Setups of Sand Specimens." *Journal of Materials in Civil Engineering* 29, no. 10 (June): 04017157. https://doi.org/10.1061/(asce)mt.1943-5533.0001985

Tekscan. 2023. "FlexiForce™ Standard Force Sensors." Tekscan. https://web.archive.org/web/20240316002820/https://www.tekscan.com/force-sensors

Tory, A. C. and R. W. Sparrow. 1967, "The influence of diaphragm flexibility on the performance of an earth pressure cell." *Journal of Scientific Instruments* 44, no. 9 (February): 781-785. https://doi.org/10.1088/0950-7671/44/9/333

USBR. 1996. *Geotechnical Training Manual No. 7: Pipe Bedding and Backfill.* USBR 1996. Denver, CO: United States Department of the Interior Bureau of Reclamation, Technical Service

Center Geotechnical Services, approved 1996. https://web.archive.org/web/20240319181238/https://usbr.gov/tsc/techreferences/mands/mands-pdfs/pipebed.pdf

Weidlich, I. and M. Achmus. 2008, "Measurement of Normal Pressures and Friction Forces Acting on Buried Pipes Subjected to Cyclic Axial Displacements in Laboratory Experiments." *Geotech. Test. J* 31, no. 4 (February): 334-343. https://doi.org/10.1520/GTJ100804

WSD. 2012. *Manual of mainlaying practice.* WSD 2012. Hong Kong SAR, China: Water Supplies Department, approved August 18, 2023. https://web.archive.org/web/20240319180712/https://www.wsd.gov.hk/filemanager/en/content_1456/Manual_of_Mainlaying_Practice_Amendment_1_2023%28finalized%29.pdf

WSD. 2020. *Guidelines for Excavation Near Water Mains.* WSD 2020. Hong Kong SAR, China: Water Supplies Department, approved December 29, 2020. https://web.archive.org/web/20240319180608/https://www.wsd.gov.hk/filemanager/en/content_1454/excavateguide.pdf

TABLE 1 Sand properties

Soil parameter	Value
Specific gravity, G_s	2.68
Particle size: mm	0.25~0.5
Median particle size, d_{50}: mm	0.375
Maximum void ratio, e_{max}	0.797
Minimum void ratio, e_{min}	0.526
Target relative density, I_D: %	85
Dry unit weight at target relative density, γ': kN/m^3	17.0
Peak friction angle: °	39.6
Critical state friction angle: °	32.8

TABLE 2 DEM simulation parameters

Simulation parameter	Value
Particle density: kg/m^3	2 680
Particles Young's modulus: MPa	150
The ratio of shear to normal stiffness of particles	0.2
Particles contact friction angle: °	34
Sensor and boundary walls Young's modulus: MPa	19 000
The ratio of shear to normal stiffness of the sensor wall	0.7
Sensor walls contact friction angle: °	10
Boundary walls contact friction angle: °	0
Target relative density, I_D: %	85
Damping ratio	0.7

TABLE 3 Pipe properties

Pipe parameter	Value
Diameter, D: mm	102
Thickness: mm	4
Total length: m	1.25
Testing length: m	0.7
Steel density: kg/m^3	7 930
Young's modulus, E: MPa	204
Poisson's ratio	0.3
Surface treatment method	Turning surface
Maximum height on the surface profile, R_{max}: mm	0.38
Normalized surface roughness, R_n	1.01
Peak interface friction angle: °	37.9
Critical state interface friction angle: °	33.5

Fig. 1 Design of TPS-based sensors: (a) schematic side view of TPS-based EPC; (b) photograph of TPS-based EPC; (c) schematic side view of TPS-based ICPT; (d) photograph of TPS-based ICPT

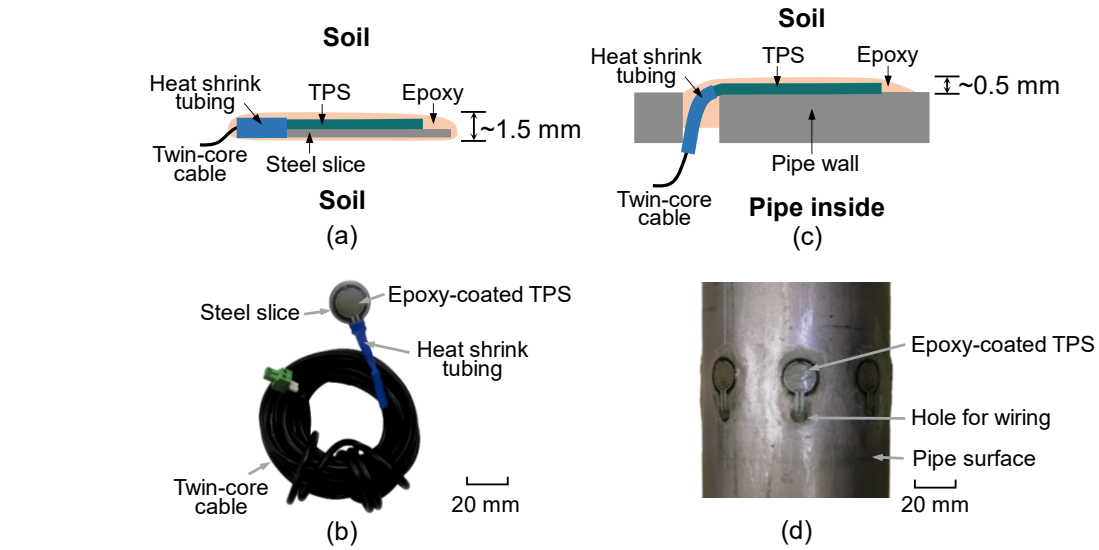

Fig. 2 Measurement wiring and method: (a) method I: resistance-voltage conversion by electrical interface; (b) method II: 4-wire electrical resistance measurement by dataTaker DT85

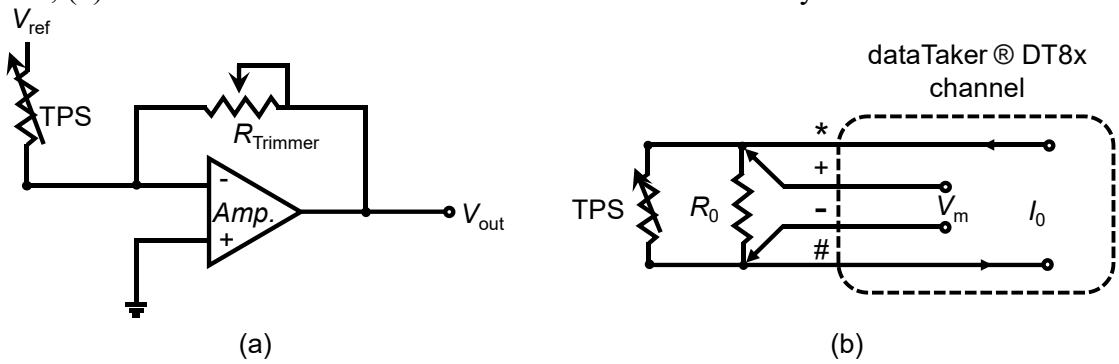

Fig. 3 Proposed calibration method of TPS-based ICPT: (a) photograph; (b) schematic diagram of internal details

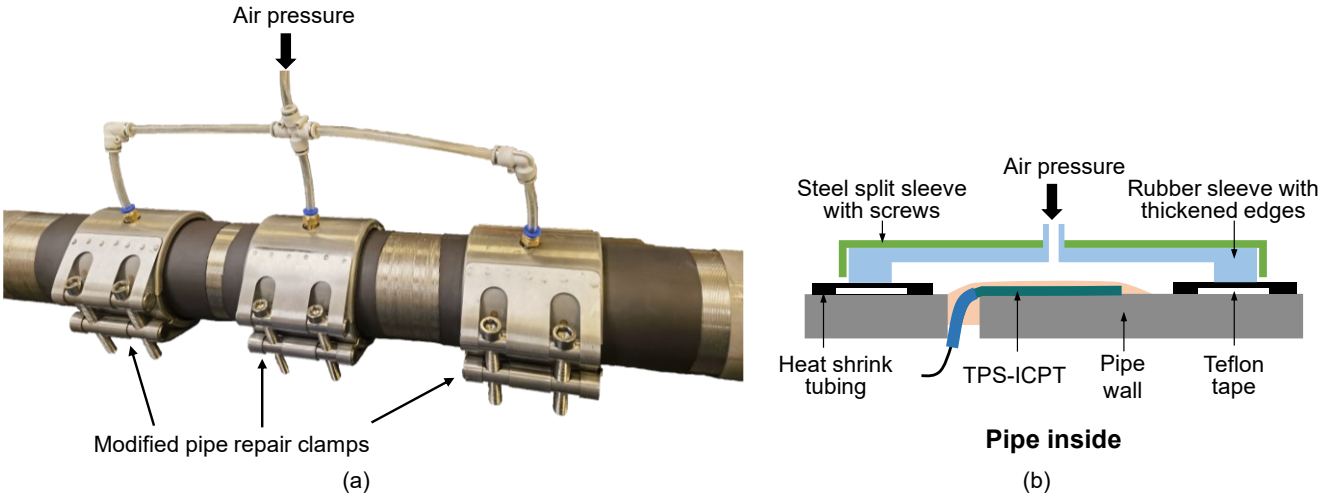

Fig. 4 Typical calibration result (Loading path: 0~200 kPa; Unloading path: 200~0 kPa; 17 stages in total; 4 kPa/min)

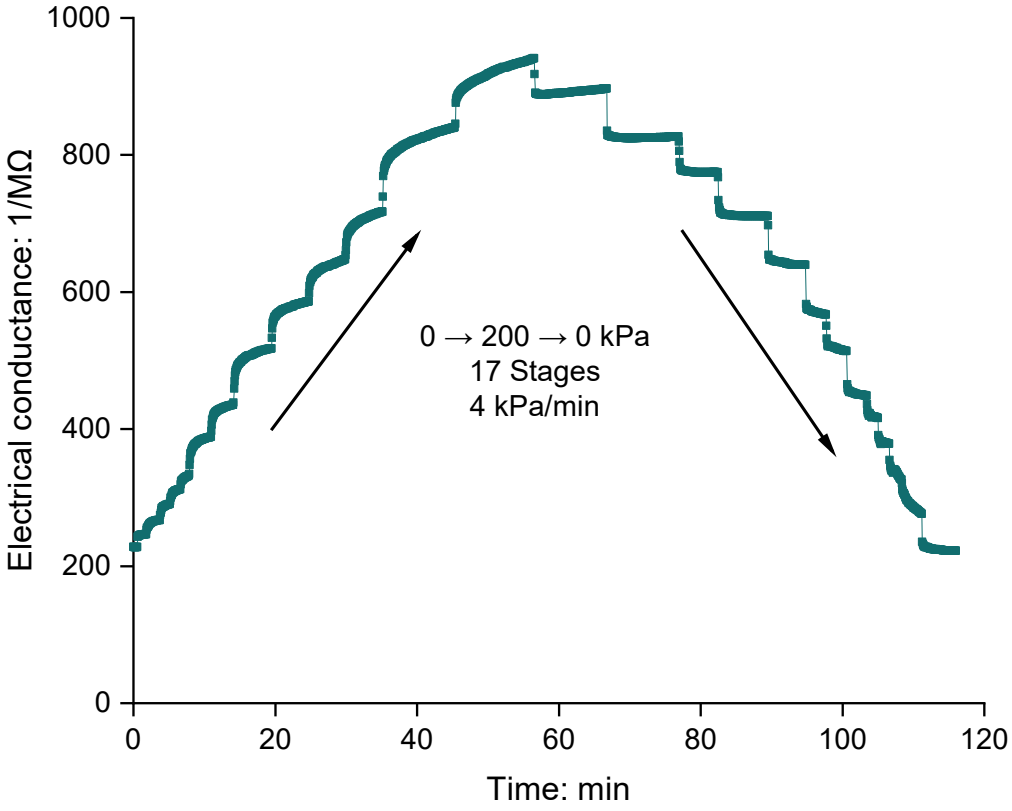

Fig. 5 Non-linearity error of TPS-based sensor (number of TPS-ICPT=15, number of TPS-EPC=3, 4 kPa/min, error bar of Y-axis = ± standard error of the mean): (a) typical air pressure - electrical conductance relationship in loop path; (b)non-linearity error vs. maximum pressure

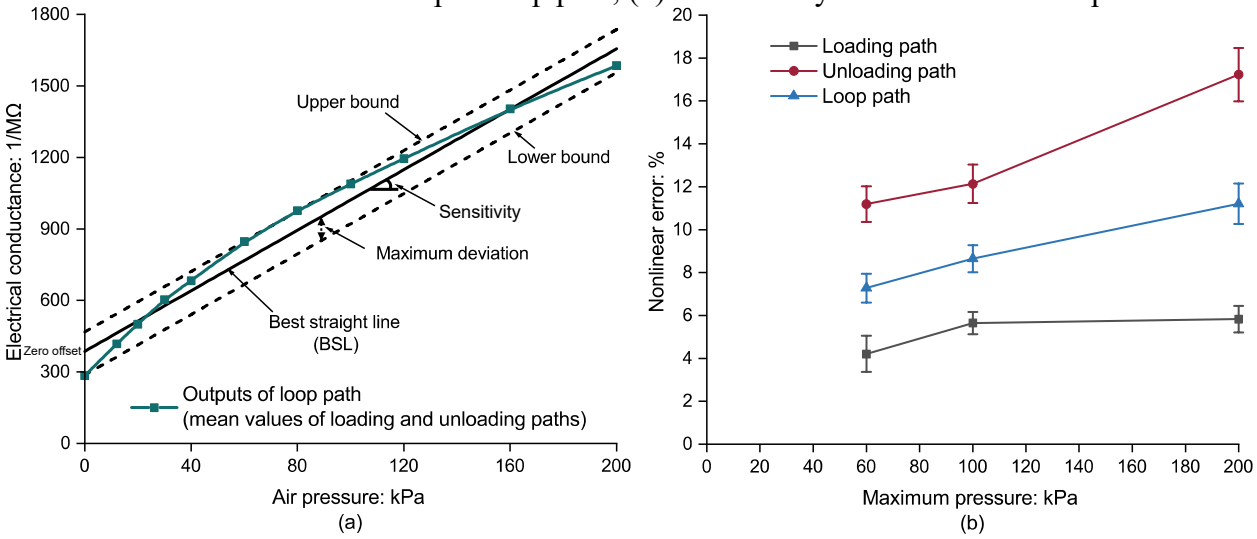

Fig. 6 Hysteresis errors of TPS-based sensor (number of TPS-ICPT=15, number of TPS-EPC=3, 4 kPa/min, error bar of Y-axis = ± standard error of the mean): (a) typical air pressure - electrical conductance relationship in loading and unloading paths; (b) hysteresis error vs. maximum pressure

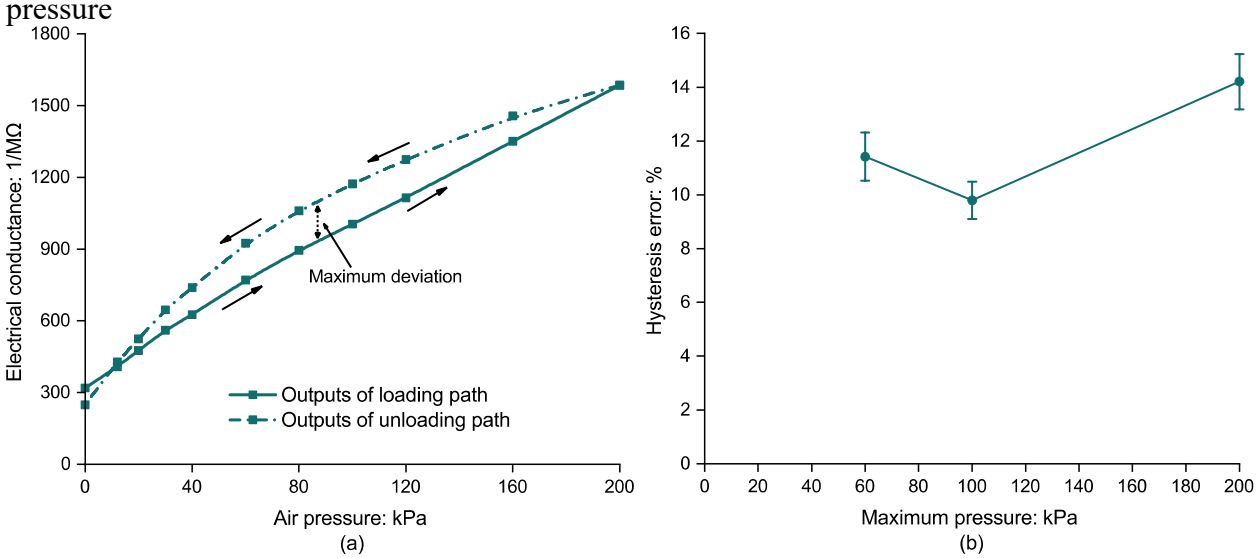

Fig. 7 Influence of loading rate on pressure-electrical conductance relationship (number of TPS-ICPT=15, number of TPS-EPC=3)

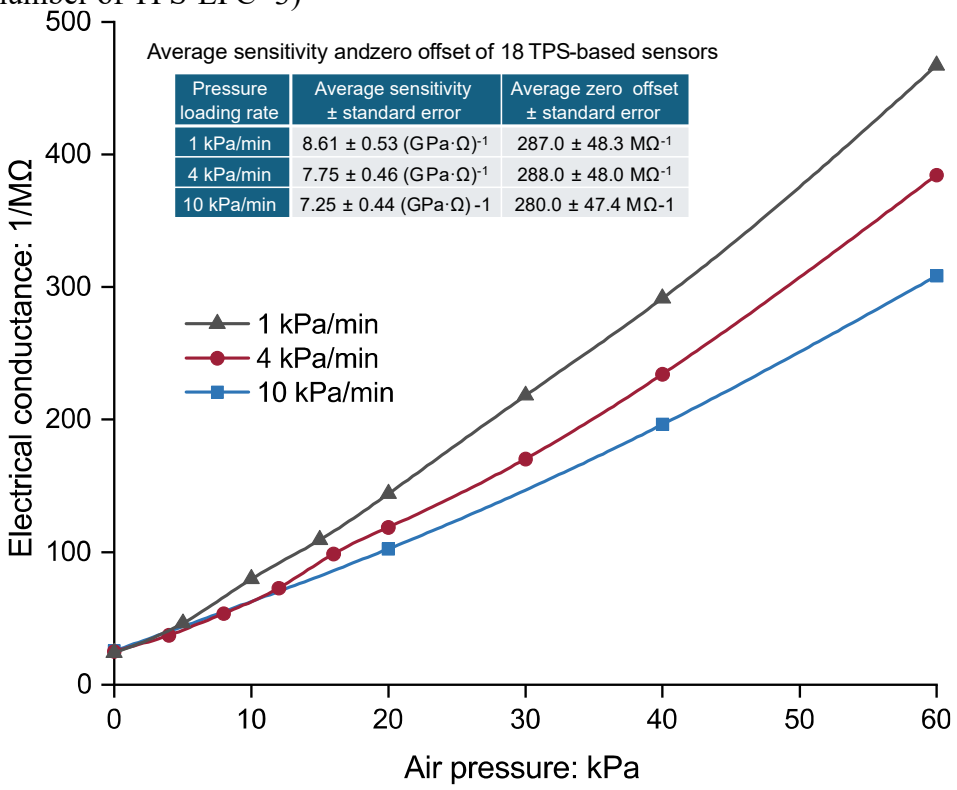

Fig. 8 Comparison between TPS-based EPC and traditional EPC in the oedometer

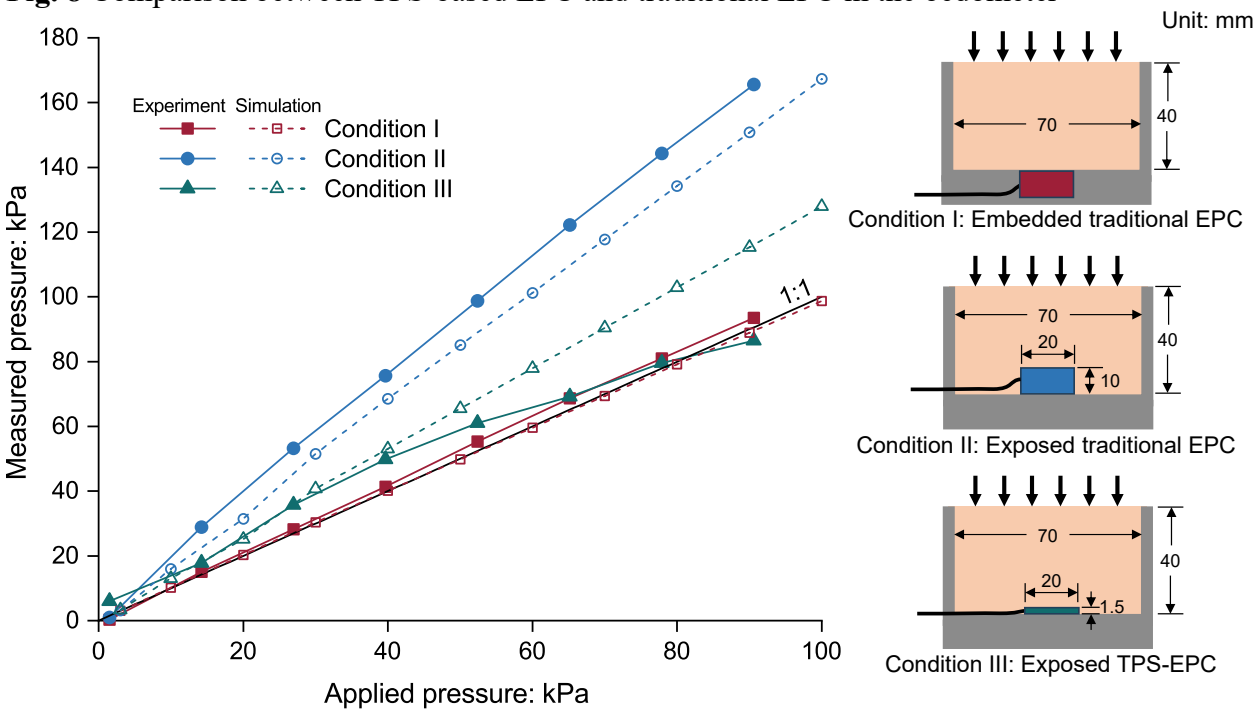

Fig. 9 Vertical displacement with applied pressure increasing from 0 to 100 kPa in DEM simulation: (a) Condition I; (b) Condition II; (c) Condition III

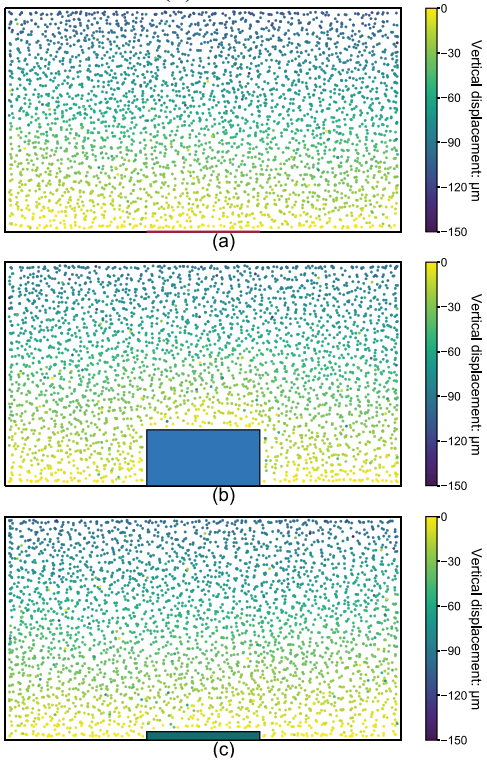

Fig. 10 force chain network with the applied pressure of 100 kPa in DEM simulation: (a) Condition I (the maximum contact normal force = 2.12 N); (b) Condition II (the maximum contact normal force = 3.08 N); (c) Condition III (the maximum contact normal force = 2.16 N)

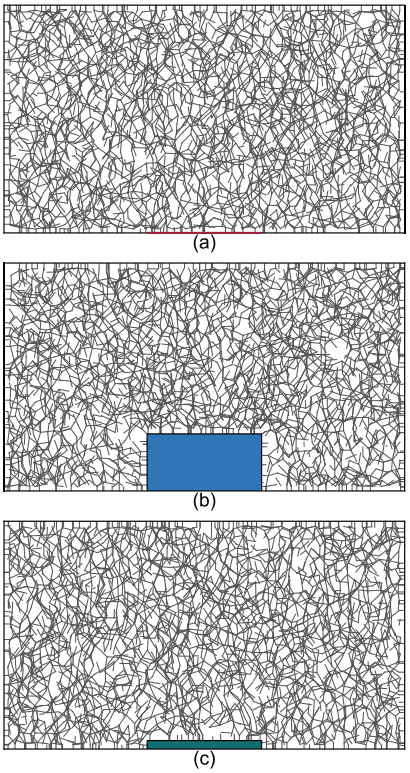

Fig. 11 Experimental system schematic diagram (modified from Guo and Zhou, 2024)

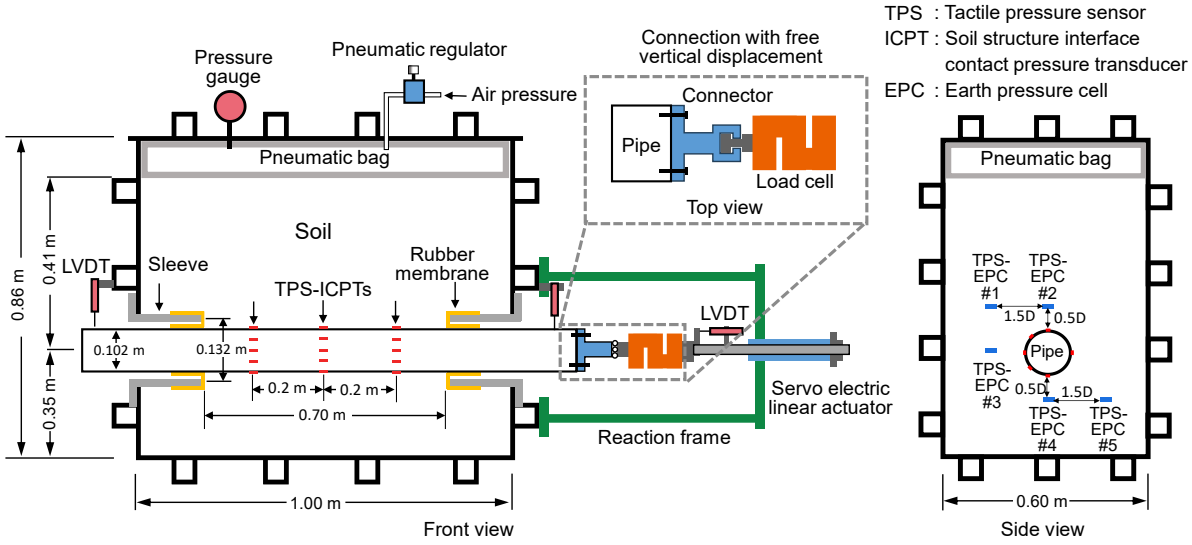

Fig. 12 Evolution of interface contact pressures measured by TPS-ICPTs

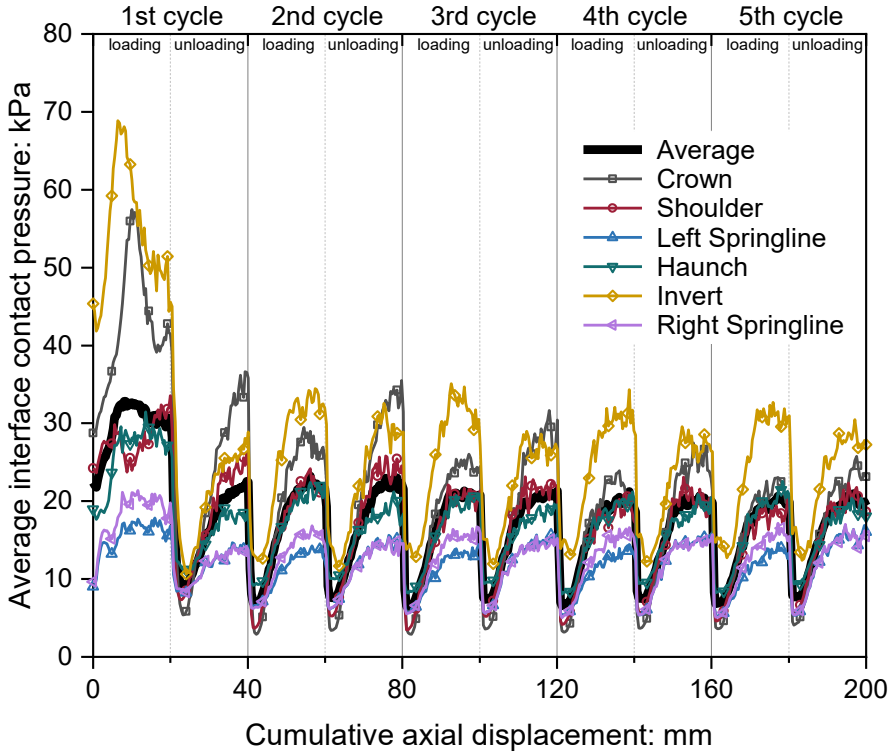

Fig. 13 Stress path based on the average interface contact pressure measured by TPS-ICPTs

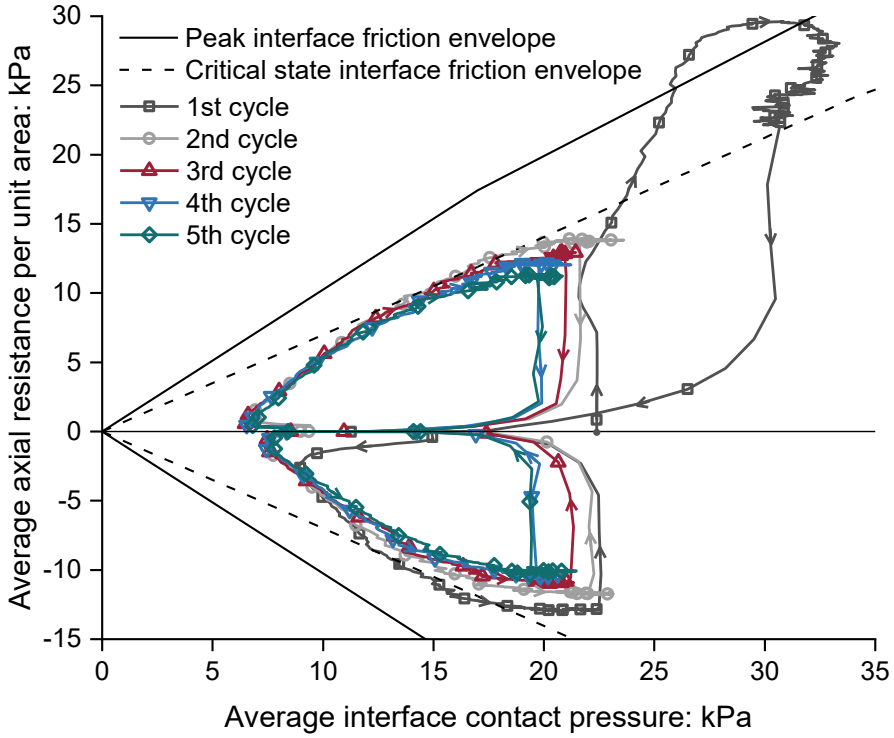

Fig. 14 Comparison between TPS-based EPC and traditional EPC in physical modeling: (a) top (position #1); (b) bottom (position #2); (c) left (position #3); (d) top left (position #4)